Solar Energy Materials & Solar Cells 155 (2016) 155–165

Contents lists available at ScienceDirect

Solar Energy Materials & Solar Cells

journal homepage: www.elsevier.com/locate/solmat

Imbalanced charge carrier mobility and Schottky junction induced anomalous current-voltage characteristics of excitonic PbS colloidal quantum dot solar cells

Lilei Hu [a], Andreas Mandelis [a,b,*], Xinzheng Lan [b], Alexander Melnikov [a], Sjoerd Hoogland [b], Edward H. Sargent [b]

[a] Center for Advanced Diffusion-Wave and Photoacoustic Technologies (CADIPT), Department of Mechanical and Industrial Engineering, University of Toronto, Toronto, Ontario, Canada M5S 3G8

[b] Edward S. Rogers Sr. Department of Electrical and Computer Engineering, University of Toronto, Toronto, Ontario, Canada M5S 3G4

ARTICLE INFO

Article history:
Received 12 March 2016
Received in revised form
6 June 2016
Accepted 7 June 2016
Available online 15 June 2016

Keywords:
Colloidal quantum dot solar cells
Photovoltaic
Exciton
Hopping mobility
Schottky diode
Heterojunction

ABSTRACT

Anomalous current-voltage (I-V) characteristics, as reported with increasing frequency, can significantly compromise the energy conversion efficiency of colloidal quantum dot (CQD) solar cells. This paper applied a purely hopping transport model rather than the traditional Schottky-diode equation to interpret the anomalous I-V curves measured in CQD solar cells with a structure: ITO/ZnO/PbS-TBAI QD/PbS-EDT QD/Au. Anomalous I-V curves were found at temperatures below 300 K. A double-diode-equivalent electric circuit was developed for the quantitative analysis of these anomalous I-V curves, yielding multiple hopping transport parameters, such as hopping diffusivity, diffusion length, mobility, and lifetime. Quantitative analysis revealed that the imbalanced charge carrier mobility in the carrier transport (PbS-TBAI) and extraction (PbS-EDT) layers, as well as the existence of a reverse Schottky diode at the PbS-EDT/Au interface, played key roles in the formation of the anomalous I-V curves. Furthermore, charge-transfer (CT) states, located at the ZnO/PbS-TBAI interface, were found to reduce the CQD solar cell open-circuit voltage through radiative and non-radiative recombination of excitons. A modified Einstein equation was also validated, further proving the presence of a Schottky barrier and pointing to a rate determining interface for the I-V behaviors of our solar cells.

1. Introduction

Colloidal quantum dots (CQDs) have attracted much attention in the past few years due to two major advantages: a) their solution fabrication process that provides possibilities for low-cost, light weight, flexible, and roll-to-roll processed electronics [1–6]; and b) tunable optical and electrical properties through feasible quantum dot size control [7–10]. As a result, CQD-based solar cells have emerged as one of most promising photovoltaic devices ever since they were first reported in 2005 [11]. In the meantime, their power conversion efficiency (PCE) and in-air stability have been significantly improved under intensive development; for example, recently researchers have successfully demonstrated respectable long-term air-stability (~5 months) for a double-QD layer solar cell architecture [12]. Our group was also successful in driving the highest current CQD solar cell PCE to 10.7% [13]. Both of these milestones are crucial in evaluating its commercial potential, further encouraging the photovoltaics community. Specifically, there are three dominant CQD solar cell architectures: Schottky-diode, heterojunction, and CQD sensitized solar cells [14]. Compared with the other two architectures, for Schottky-diode based CQD solar cells, given a short-circuit current density (J_{sc}), device efficiency is diminished by the lower Fill Factor (*FF*) and open-circuit voltage (V_{oc}) which are due to a poor energy barrier for hole injection into the electron-extraction electrode [14]. Furthermore, in CQD sensitized solar cells, charge transport is facilitated due to the micrometer-thick matrix, however, light absorption efficiency is reduced as a consequence of this thin layer of light absorber on a high surface area electrode [14]. In comparison, heterojunction based CQD solar cells are much better with respect to the final device energy conversion efficiency, as they can simultaneously maximize *FF*, V_{oc} and I_{sc} as well as light absorption efficiency through proper material energy band engineering and

* Corresponding author at: Center for Advanced Diffusion-Wave and Photoacoustic Technologies (CADIPT), Department of Mechanical and Industrial Engineering, University of Toronto, Toronto, Ontario, Canada M5S 3G8.
E-mail address: mandelis@mie.utoronto.ca (A. Mandelis).

http://dx.doi.org/10.1016/j.solmat.2016.06.012
0927-0248/

optimization of the light-absorption layer thickness [14]. Exciton hopping transport in CQD solar cells involves exciton diffusion and dissociation distinct from charge transport mechanisms which govern conventional inorganic silicon cells [7]. However, most studies of CQD solar cells to-date are based on the classical Schottky diode equation that was derived under the assumption of continuous energy band semiconductor systems where electron-hole pairs dissociate immediately upon their generation and travel at high charge mobility. Crystalline Si is representative of these photovoltaic materials whereas CQD and organic solar cells are excluded from that category [15,16]. Würfel, et al. demonstrated that the Schottky equation cannot be applied to low-mobility materials in the way it is used for inorganic solar cells, and device parameters extracted from the Schottky equation such as ideality factor, series resistances and shunt resistance lack real physical meaning [17] and provide very limited assistance toward the optimization of device fabrication. In comparison, material parameters including carrier mobilities, diffusion length, lifetime, diffusivity, and trap states offer more important information for solar cell device structure optimization, starting with selection of materials. Unfortunately, in common with organic photovoltaic materials, CQDs constitute low carrier mobility photovoltaic materials and have high exciton binding energy, both impediments to improving solar efficiency in a straightforward manner. In summary, a full understanding of charge carrier transport mechanism within CQD devices is lacking.

Another impediment to solar cell device efficiency is the formation of a Schottky junction at the CQD/anode interface which forms an electric field with direction opposite to that of the light incidence. This Schottky junction causes holes to accumulate at the CQD/anode interface [16,18], thereby reducing the surface recombination velocity (SRV) as observed in organic photovoltaic devices [19]. All of these adverse processes handicap hole extraction at the anode and lead to low solar conversion efficiency. An experimental consequence of hole accumulation is the formation of anomalous (including S-shaped) current-voltage (I-V) curves, which have been reported for heterojunction CQD solar cells with increasing frequency [12,15,20]. Nevertheless, the origins of the formation of these anomalous I-V curves have not been well understood, nor have they been exploited toward designing higher performance solar cells. Wang et al. [21] attributed them to the electron accumulation effect induced by an exciton blocking layer. Wagenpfahl et al. [19] found the reduction of hole-associated surface recombination velocities could also give rise to S-shaped I-V curves. One approach to study S-shaped I-V curves is through fitting experimental data to theoretical electric circuit models. However, although Romero et al. [22] developed equivalent electric circuit models that can quantitatively simulate three kinds of I-V curves in terms of forward and reverse diodes, they did not consider actual physical mechanisms. Here we analyze the temperature-dependent I-V characteristics using a double-diode electric circuit model and a hopping transport model to explain their origins. In addition, performance factors of our device architecture are discussed with improvement recommendations.

2. CQD solar cell fabrication and I-V measurement

PbS CQDs were prepared following our previous reports [23,24]. Briefly, oleic acid (4.8 mmol), PbO (2.0 mmol) and 1-octadecence (ODE, 56.2 mmol) were mixed and heated to 95 °C under vacuum. This was followed by the injection of bis(trimethylsilyl) sulphide and ODE at a high temperature of 120 °C. After cooling, the PbS CQDs were successively precipitated and redispersed using acetone and toluene, respectively. The products were stored in a nitrogen glovebox for further surface passivation treatments. CQD solar devices fabricated in this manner have the structure of ITO/ZnO/PbS-TBAI QD/PbS-EDT QD/Au which has been demonstrated by two groups to be stable for ca. 5 months [12], and at least 1 month [13], respectively. S-shaped I-V curves at room temperature for a CQD solar cell with this structure were also reported by Chuang et al. [12] but were not well-understood in terms of physical optoelectronic processes. Devices were fabricated in air through a typical solution process [12,23,25]. TBAI and EDT denote tetrabutylammonium iodide and 1, 2-ethanedithiol, respectively. They are exchange-ligands for PbS CQDs to passivate quantum dot surface trap states and adjust the interdot distance which determines the coupling strength between two neighboring dots. The exciton transition energy (effective band gap) of PbS QD was measured in a solid CQD nanolayer to be ca. 1.4 eV. In the fabrication process, a ca.100-nm ZnO nanoparticle layer was spin-coated onto a clean glass substrate with a pre-deposited ITO electrode of 145 nm thickness. PbS QD layers were deposited through a layer-by-layer spin-coating process, after which a TBAI solution (10 mg/ml in methanol) was applied to the substrate for 30 s, followed by successive methanol rinse-spin steps. An EDT solution (0.01 vol% in acetonitrile) and acetonitrile were used for the deposition of the PbS-EDT nanolayer. As examined by scanning electron spectroscopy, the final thicknesses of PbS-TBAI and PbS-EDT were ca. 200 nm and 50 nm, respectively. In addition, a 120-nm-thick Au anode was evaporated on the top of PbS-EDT. Fig. 1 shows a schematic of the fabricated CQD solar cell. Its energy diagram is shown in Fig. 2 which illustrates that, under illumination, excitons generated in PbS-TBAI dissociate into free electron and hole carriers through interdot coupling strength and the electric field at the heterojunction interface. Free-electrons are swept onto the cathode within the depleted area. In addition, because of the energy barrier formed at the PbS-TBAI/PbS-EDT interface, electrons are blocked from flowing to the anode which can significantly increase I_{sc} and V_{oc} [12,25]. Unfortunately, as will be discussed later, such architecture leads to the formation of a Schottky barrier in PbS-EDT, which prevents holes from being extracted to the external Au anode, resulting in hole accumulation and formation of an electric field with reverse direction to the forward field in the main heterojunction diode (PbS-TBAI/ZnO). In the following discussion, for the sake of clarification, the subscript *h* refers to the heterojunction diode (ZnO/PbS-TBAI) and *s* refers to the Schottky diode (PbS-EDT/Au). Fig. 3 shows the equivalent circuit: two diodes with opposite electric field directions representing heterojunction and Schottky diode, respectively.

The homojunction formed at the PbS-TBAI/PbS-EDT interface gives rise to an electric field with forward direction, same as that of the heterojunction, but its strength is diminished by the reverse Schottky barrier because of the low PbS-EDT layer thickness (50 nm). Therefore, to simplify the analysis and improve

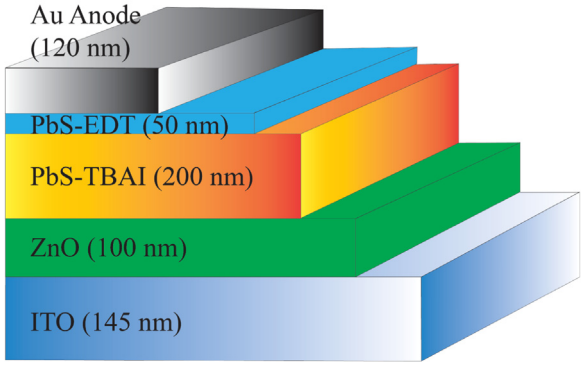

Fig. 1. Schematic of double-layer CQD solar cell with the structure: ITO/ZnO/PbS-TBAI QD/PbS-EDT QD/Au.

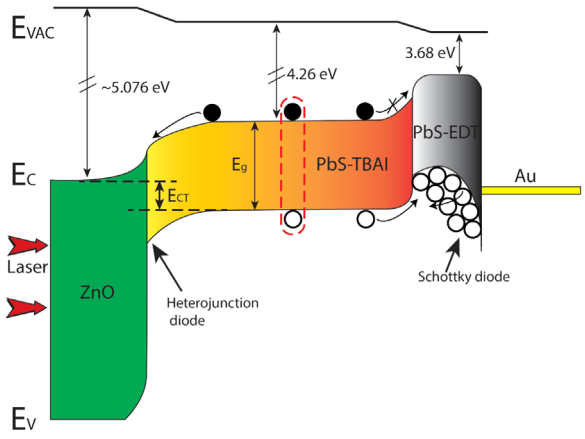

Fig. 2. Device energy band diagram under illumination. PbS-EDT acts as an electron blocking layer and a Schottky barrier is formed for holes, thus prevent their extraction to the Au anode.

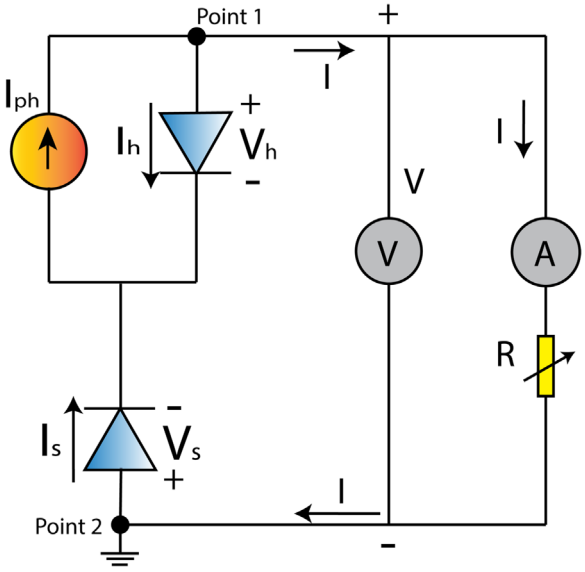

Fig. 3. Equivalent electric circuit of a double-diode model, consisting of a heterojunction diode between ZnO and PbS-TBAI layers and a Schottky diode between PbS-EDT and Au.

parameter fitting reliability by decreasing the number of unknown parameters in the hopping transport theoretical model developed [26] and used in this work, this homojunction is not considered as an independent diode in this paper, but part of the heterojunction.

The I-V characteristic curve measurements were obtained under laser excitation with wavelength of 830 nm and excitation intensity of 100 mW/cm^2. The sample was placed on a Linkam LTS350 cryogenic stage which can maintain a constant temperature in a range from 77 K to 520 K. For this study, the I-V characterizations were performed at 300 K, 250 K, 200 K, 150 K, and 100 K.

3. Theory and calculation

3.1. Double-diode-equivalent hopping transport model

CQD solar cell I-V curves can be quantitatively interpreted using a hopping transport mechanism [26]. Referring to the energy diagram in Fig. 2, any hole accumulation at the PbS-EDT/Au interface due to the effective impedance presented by the Schottky barrier can give rise to a local space charge layer (SCL) W and an electric field with opposite direction to the heterojunction electric field. Therefore, charge carrier hopping transport in PbS-TBAI (heterojunction) dominated by electron transport, and in PbS-EDT (Schottky barrier) dominated by hole transport, should be distinct. Influence of the Schottky barrier on the net current density is expected to be strong and possibly dominant over the local diffusion current density due to the thinness of the SCL, especially at low temperatures. To extract carrier hopping transport parameters, the electron current across the heterojunction is expressed as the sum of diffusion and drift currents [26]:

$$I_h = qAN_0\left\{\left[\frac{D_h(T)}{L_h(T)}\right]\left(\frac{\cosh\left[d/L_h(T)\right]}{\sinh\left[d/L_h(T)\right]}\right)+\mu_h(T)E_h\right\}\left(\exp\left[\frac{\mu_h(T)V_h}{D_h(T)}\right]-1\right) \quad (1)$$

Here, q is the elementary charge, A is the CQD solar cell area exposed to the light, N_0 is the electron/hole population at equilibrium, $D_h(T)$ is the electron hopping diffusivity, $L_h(T)$ is the electron diffusion length, d is the CQD layer thickness, μ_h is the electron hopping mobility in PbS-TBAI corresponding to the heterojunction, $V_h$is the electric potential across the entire heterojunction, and E_h is the electric field. According to this mechanism, the heterojunction gives rise to an electric field across the entire CQD nanolayer, while the Schottky diode generates a reverse electric field in the local SCL with a nominal thickness of$W$. Similarly, as a combination of diffusion and drift currents the hole current flowing across the Schottky diode can be expressed as [26]:

$$I_s = qAN_0\left\{\left[\frac{D_s(T)}{L_s(T)}\right]\left(\frac{\cosh\left[(d-W)/L_s(T)\right]}{\sinh\left[(d-W)/L_s(T)\right]}\right)+\mu_s(T)E_s\right\}\left(\exp\left[\frac{\mu_s(T)V_s}{D_s(T)}\right]-1\right) \quad (2)$$

All parameters are analogous to those of the heterojunction in Eq. (1), while it is noted that E_s is the electric field associated with the Schottky diode.

The analysis of the double-diode electric circuit model of Fig. 3 yields

$$V = V_h - V_s \text{ and at point 1, } I_{ph} = I + I_h. \text{ At point 2, } I = I_s, \text{ therefore, } I_{ph} = I_s + I_h \quad (3)$$

Using Eqs. (1)–(3), the external voltage V can be written as a function of the external current I and the free charge carrier hopping transport parameters:

$$V = \frac{D_h(T)}{\mu_h(T)}ln\left\{\frac{I_{ph}-I}{qAN_0\left[\frac{D_h(T)}{L_h(T)}\frac{\cosh\left[\frac{d}{L_h(T)}\right]}{\sinh\left[\frac{d}{L_h(T)}\right]}+\mu_h(T)E_h\right]}+1\right\} - \frac{D_s(T)}{\mu_s(T)}ln\left\{\frac{I}{qAN_0\left[\frac{D_s(T)}{L_s(T)}\frac{\cosh\left[\frac{d}{L_s(T)}\right]}{\sinh\left[\frac{d}{L_s(T)}\right]}+\mu_s(T)E_s\right]}+1\right\} \quad (4)$$

A hallmark of the hopping transport nature of charge carriers in

the CQD architecture of Fig. 2 based on quantum dot-to-dot hopping and transport across the PbS-TBAI and the PbS-EDT interfaces, is a modified Einstein relation compared to the conventional continuous-band solar cells. The theory of quantum dot-to-dot carrier hopping and transport across discontinuous energy interfaces such as the Schottky barrier leads to an Einstein relation which takes on the "hopping" activation form [26]:

$$\frac{\mu_j(T)}{D_j(T)} = \left(\frac{q}{nkT}\right) exp\left(-\frac{E_{a,j}}{kT}\right) \tag{5a}$$

where $j=h(s)$ denotes the heterojunction (Schottky) interface, n is the dimensionality of the problem, and $E_{a,j}$ is the activation energy of the respective barrier (barrier height). This parameter originates in the mobility component in Eq. (5a) which is the effective mobility, the externally measured transport property of carriers into which excitons are dissociated. The Boltzmann factor $exp(-E_{a,j}/kT)$ appears in the Einstein relation (5a) due to the fact that carriers (holes in this case, Fig. 2) hop to thermally cross over the CQD-PbS-EDT/Au barrier $E_{a,j}$, to enter the external circuit used for the measurement. The mobility being the externally measured transport quantity carries this hopping factor, whereas the diffusivity is a transport property internal to the CQD active layer and is not subject to the interfacial hopping probability. Eq. (5a) assumes that inter-quantum dot hopping is an exponentially thermally activated process with a hopping time constant given by [2].

$$\frac{1}{\tau_j(T)} = \frac{1}{\tau_{0,j}} exp\left(-\frac{E_{ij}}{kT}\right) \tag{5b}$$

Here, the quantity $\tau_{0,j}$ is a characteristic time for hopping of carriers (excitons or their dissociation product charge carriers) between nearest neighbor quantum dots crossing an inter-dot energy barrier E_{ij} over a distance x_{ij} that separates the two quantum dots at locations (i) and (j). $\tau_{0,j}$ is temperature independent and given by [27].

$$\frac{1}{\tau_{0,j}} = f exp(-\gamma_{ij} x_{ij}) \tag{5c}$$

where f is an attempt frequency and γ_{ij} is related to the hopping probability across the energy barrier of effective thickness/distance x_{ij}. The foregoing Einstein relation (5a) was experimentally validated in the case of a depleted heterojunction PbS CQD solar cell [26]. It was also be tested and found to be valid in the present device structure in this paper.

3.2. Origins of anomalous current-voltage curves

Experimental I-V curves measured on a typical CQD solar cell under illumination exhibit temperature-dependent shapes, i.e. I-V curves change from exponential (300 K), to S-shaped (250 K and 230 K), and to negative exponential (200 K,150 K and 100 K), as shown in Fig. 4. Tress et al. [28] found that S-shaped I-V curves were induced by strongly imbalanced minority charge carrier mobilities (hole mobility in excess donor, and electron mobility in excess acceptor regions) in organic solar cells. As a consequence, the *FFs* were compromised. Similarly, in the present study, imbalanced mobilities between charge carrier transport in the light absorbing layer (PbS-TBAI) and in the carrier extraction layer (PbS-EDT) were also found to alter device I-V curves due to enhanced hole accumulation which increases the Schottky diode reverse electric field strength.

To investigate the effects of imbalanced charge carrier mobilities in the PbS-TBAI and PbS-EDT, I-V curves were simulated using Eq. (4) and gradually reducing the hole mobility μ_s from 1 cm^2/Vs to 0.005 cm^2/Vs, while other hopping parameters were kept unchanged as shown in Fig. 5(a). Trial values for each parameter were selected referring to reported values for different ligand-treated PbS CQDs. Kholmicheva et al. [29] studied MOA (8-mercaptooctanoic acid), and MPA (3-mercaptopropionic acid) treated PbS CQDs using photoluminescence (PL) spectroscopy, and measured the corresponding exciton diffusivities to be 0.003 cm^2/s and 0.012 cm^2/s, respectively. Carey et al. [30] estimated free electron and hole diffusion length in the range from 30 to 230 nm for various PbS CQDs, including EDT treated, pure, $CdCl_2$ treated, bromide treated, pure fused, and solution or solid-state-iodide-treated PbS CQDs. For electron and hole mobility in CQD nanolayers used as CQD solar cell light-absorption and charge-carrier-transport layers, Carey et al. [30], and Tang and Sargent [7] tabulated hole (electron) mobilities for three types of ligand-treated PbS CQDs. PbS CQD nanolayers without further ligand treatments yielded hole (electron) mobility of 7.2×10^{-4} cm^2/Vs (1×10^{-3} cm^2/Vs for electrons), while for $CdCl_2$-treated and butylamine-treated CQD nanolayers, it was reported to be 1.9×10^{-3} cm^2/Vs (4.2×10^{-3} cm^2/Vs for electrons) and 1.5×10^{-3} cm^2/Vs (2×10^{-4} cm^2/Vs for electrons), respectively. To our best knowledge, the strength of the hetero/homojunction-induced electric field in PbS CQDs has not been reported. However, the electric field should be inversely proportional to device thickness. In InAs/GaAs QD solar cells, Kasamatsu et al. [31] reported that the electric field was 46 kV/cm when the device thickness was ca. 300 nm. This value increased to 193 kV/cm when the device thickness was reduced to 50-nm. Due to the thinness of our Schottky diode SLC, a relatively higher electric field value of 1×10^6 V/cm was chosen for simulations. To investigate the influence of hole mobility μ_s on the solar cell I-V curves, parameters common to both heterojunction and Schottky diode were considered to have the same values. Fig. 5(a) shows shape changes which are consistent with our experimental solar cell I-V curves from normal exponential, to S-shaped, to negative exponential, when μ_s decreases from 1 cm/Vs to 0.005 cm/Vs. Compared with the electron mobility μ_h in the heterojunction, a higher μ_s value for the Schottky diode facilitates the extraction of charge carriers to the external anode. As already mentioned, for this double-diode model there are four types of currents contributing to the final device current, i.e. both heterojunction and Schottky diode contribute diffusion and drift currents. Most excitons dissociate within the heterojunction (ZnO/PbS-TBAI) and the homojunction (PbS-TBAI/PbS-EDT) interfaces, where the electric fields and/or interdot coupling strength are strong enough to split bound electron-hole pairs. In addition, the diffusion current pertaining to the Schottky diode is negligibly small. As a consequence, it is expected that high μ_s can enhance hole extraction efficiency, thereby improving solar cell performance.

In contrast, when μ_s is very small, such as in the case of low hole mobility within PbS-EDT, holes accumulated at the PbS-EDT/Au interface induce a local SCL and electric field. A similar phenomenon has been reported for a depleted-heterojunction PbS CQD solar cell [26]. In the present case, the decrease of μ_s may be due to multi-phonon assisted carrier hopping in CQD nanolayers: at high temperatures, the high phonon density results in high hole mobility. Temperature-dependence of charge carrier mobility was reported before [32]. It was also found [33,34] that carrier-mobility-controlled current density increased with temperature. As shown in Fig. 5(b), the solar cell *FF* increases with μ_s and saturates above 0.2 cm^2/Vs. Saturation implies that all holes that flow to the anode metal are effectively extracted when hole mobility is high enough, however, higher hole mobility cannot improve solar cell efficiency.

For our PbS CQD solar cell the diffusion current in the Schottky diode region is negligible. To explore the influence of diffusivity, Fig. 6(a) shows that high diffusivity also gives rise to anomalous

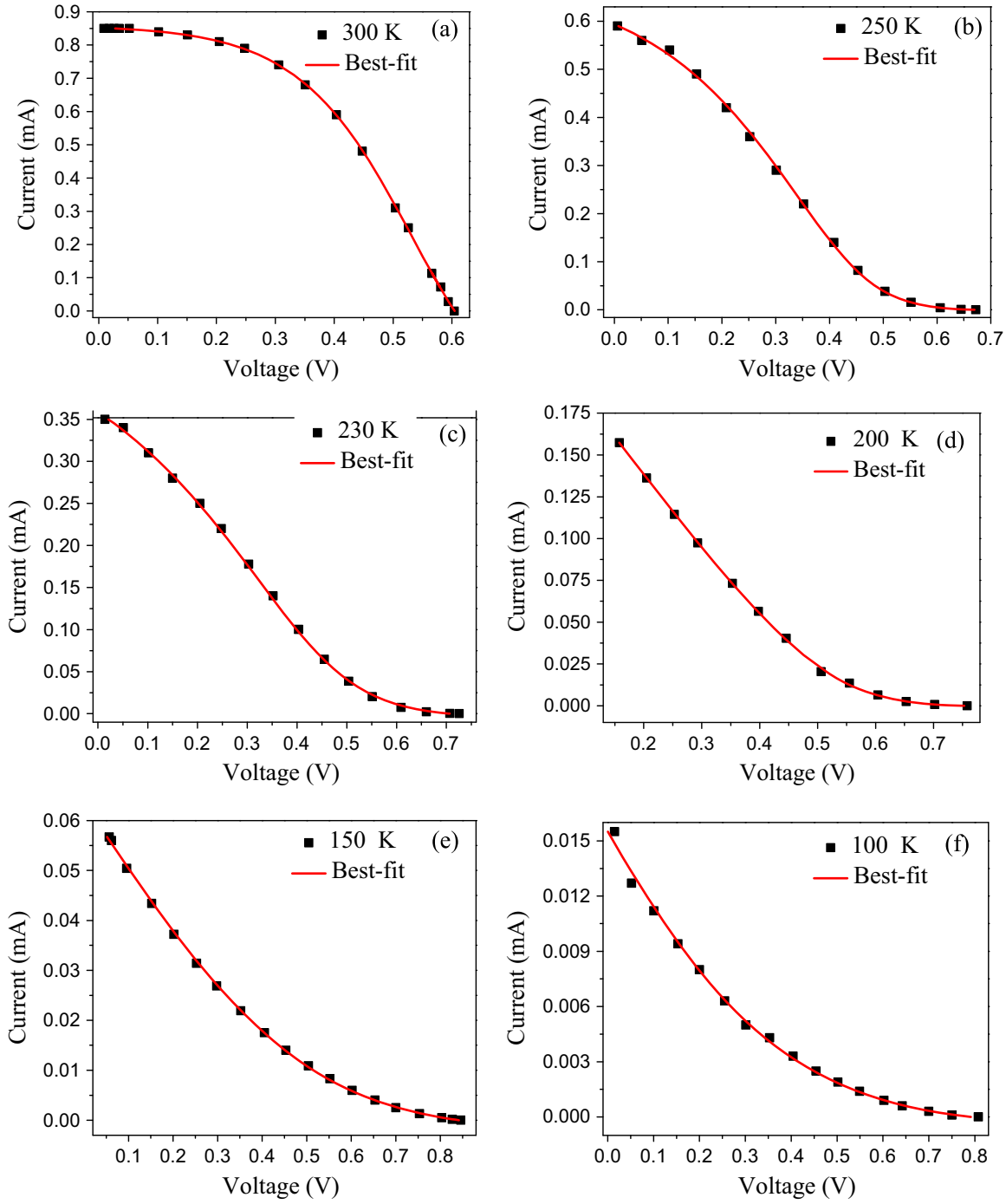

Fig. 4. I-V characteristic curves of a CQD solar cell measured at 300 K (a), 250 K (b), 230 K (c), 200 K (d), 150 K (e), and 100 K (f).

solar cell I-V curves. This simulation used the same values of all other parameters as in Fig. 5(a). High diffusion current at high diffusivity D_s compromises the one-diode heterojunction I-V behavior. Consistently, Fig. 6(b) shows *FF* decrease with increasing hopping diffusivity.

Besides imbalanced charge carrier mobility, the Schottky barrier is another key-role playing factor in the formation of anomalous CQD solar cell I-V curves. When holes arrive at the Schottky diode side, Fig. 2, they are transported to the Au anode through a phonon-assisted hopping transport mechanism. Therefore, with decreasing temperature the reduced phonon population depresses this phonon-assisted hole hopping process. As a consequence, more holes accumulate at the interface, leading to anomalous I-V curves as measured. Fig. 4(a) to (f) shows excellent match between experimental I-V curves and best fits to the theoretical model using Eq. (4).

3.3. Open-circuit voltage origin of excitonic solar cells

The Shockley-Queisser (SQ) limit [35] was derived for continuous-band semiconductors where photon interactions with a solar cell induce the generation and recombination of free electron-hole pairs. This mechanism is true for inorganic solar cells when carrier binding energy is much smaller than the thermal energy *kT*, in which case lattice-bound excitons dissociate into free electrons and holes at room temperature [36]. Consequently, V_{oc} in

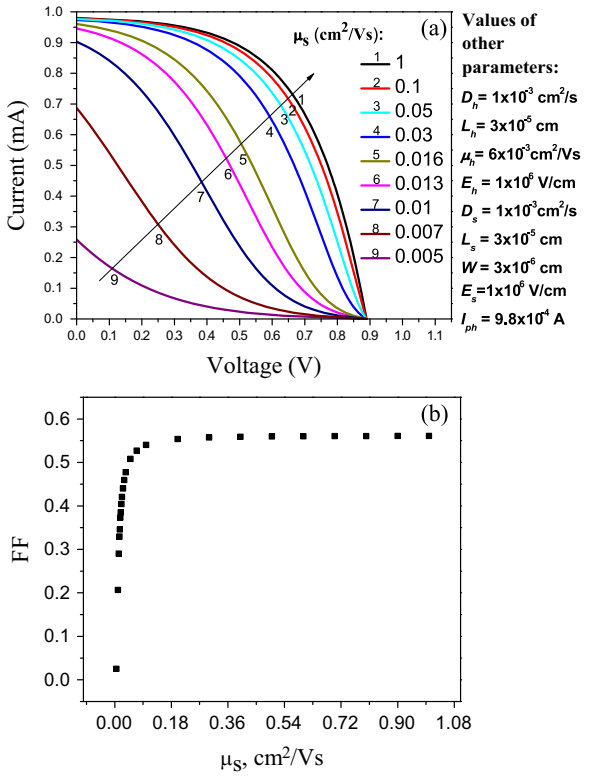

Fig. 5. (a) Current-voltage curves at various μ_s, while other parameters are kept constant, and (b) solar cell *FF* as a function of μ_s.

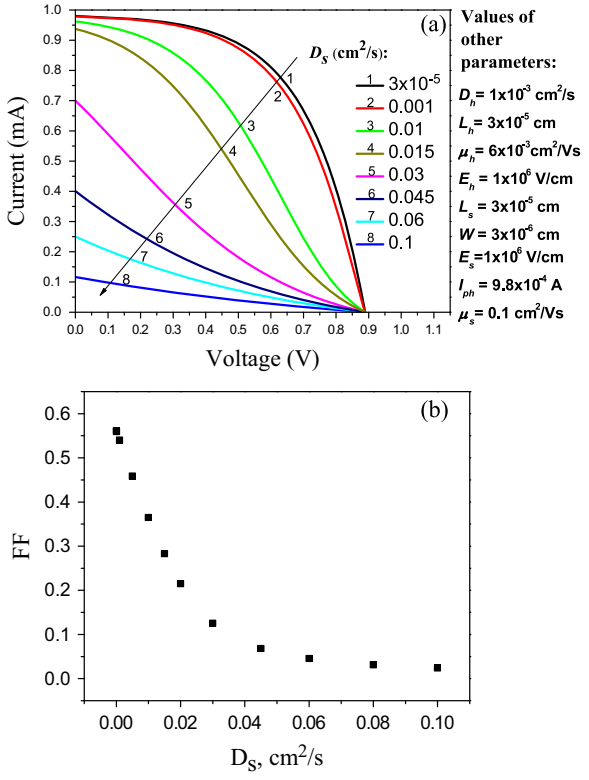

Fig. 6. (a) Current-voltage curves at various D_s, while other parameters are kept constant, and (b) solar cell *FF* as a function of D_s.

the case of ideal solar cells is the result of electron and hole quasi-Fermi energy level splitting, equal to the voltage difference between device contacts [37–39]. Carried over to CQD solar cells, use of the SQ limit requires that exciton binding energy should be negligible. This is not the case with the majority of CQD solar cells which have high exciton binding energy, especially in CQD nanolayers with low coupling strength and large interdot distances. Therefore, in most practical CQD solar cells, an exciton must encounter a heterojunction where it can dissociate into free electrons and holes. Unfortunately, heterojunctions incur additional energy losses by enhanced exciton recombination, which, in turn, decreases V_{oc} and device efficiency [40–42]. Specifically, impacts of heterojunctions on V_{oc} loss are through the formation of charge-transfer (CT) states located at acceptor-donor interfaces (the ZnO/PbS-TBAI interface in this study), a mechanism also reported for organic solar cells [40–43]. As shown in Fig. 2, E_{CT} is the energy gap between E_c of ZnO and E_v of PbS-TBAI and excitons remain electrically neutral due to their high binding energy. Hopping excitons diffuse and induce charge transfer across the heterojunction interface to form a bound polaron pair (BP) with binding energy E_B, which is significantly smaller than the binding energy of a bulk exciton. These types of bound pairs are prone to dissociating into free carriers. In the case of organic photovoltaic materials, E_B is typically less than 0.5 eV and thus results in non-thermodynamically limited exciton dissociation, always being lower than the bulk exciton binding energy (1 eV) [40]. It is known [43–45] that CT states can also absorb photons, but due to the much lower density of these interface states than bulk states, the CT absorption coefficient is typically two to three orders of magnitude lower than that inducing bulk exciton transitions [44,45]. Furthermore, because excitons are bound with smaller energy gap (E_{CT}) at the heterojunction interface than with bulk energy gap (E_g), bulk materials dominate absorption whereas heterojunction interfaces dominate recombination and dissociation. Consequently, the recombination rate increases at interfaces because it can take place via lower energy bound-pair states. Moreover, since small E_{CT} does not limit dissociation, electron and hole quasi-Fermi energy level splitting is no longer the major factor in determining V_{oc}. The maximum possible open-circuit voltage is determined by $qV_{oc}^{max} = E_{CT}$, which occurs in the limit of high-incident intensity and 0 K [40]. V_{oc} is proven to be temperature-dependent and can be expressed by the following expression [41,43].

$$V_{oc}(T) = \frac{E_{CT}}{q} + \frac{kT}{q} ln\left[\frac{J_{sc} h^3 c^2}{fq2\pi(E_{CT} - \lambda)}\right] + \frac{kT}{q} ln(EQE_{EL}), \quad (6)$$

where J_{sc} is the short-circuit current density, h is Plank's constant, f is the florescence emission intensity, λ is the reorganization energy associated with the CT absorption process, and EQE_{EL} is the electron luminescence external quantum efficiency. V_{oc} losses occur through radiative and non-radiative CT state recombination, labeled as ΔV_{OC}^{rad} and ΔV_{OC}^{non}, respectively. V_{oc} loss to radiative CT state recombination (ΔV_{OC}^{rad}) is a thermodynamically imposed mechanism for a given material system, whereas non-radiative recombination (ΔV_{OC}^{non}) can be avoided through many approaches, for example, by removing material defects. From Eq. (6), ΔV_{OC}^{rad} and ΔV_{OC}^{non} can be obtained as [41]:

$$\Delta V_{OC}^{rad}(T) = -\frac{kT}{q} ln\left[\frac{J_{sc} h^3 c^2}{fq2\pi(E_{CT} - \lambda)}\right] \quad (7a)$$

$$\Delta V_{OC}^{non}(T) = -\frac{kT}{q} ln(EQE_{EL}) \quad (7b)$$

Fig. 7(a) shows best-fits to the temperature-dependent V_{oc} using Eq. (6). The best-fitting procedure was performed 300 times, followed by statistical analysis of the fitted parameters to generate the final parameters as summarized in Table 1. The detailed procedure to assure reliability of the measured parameters is discussed in the next section. The fitted E_{CT}=1.1 eV exhibits high

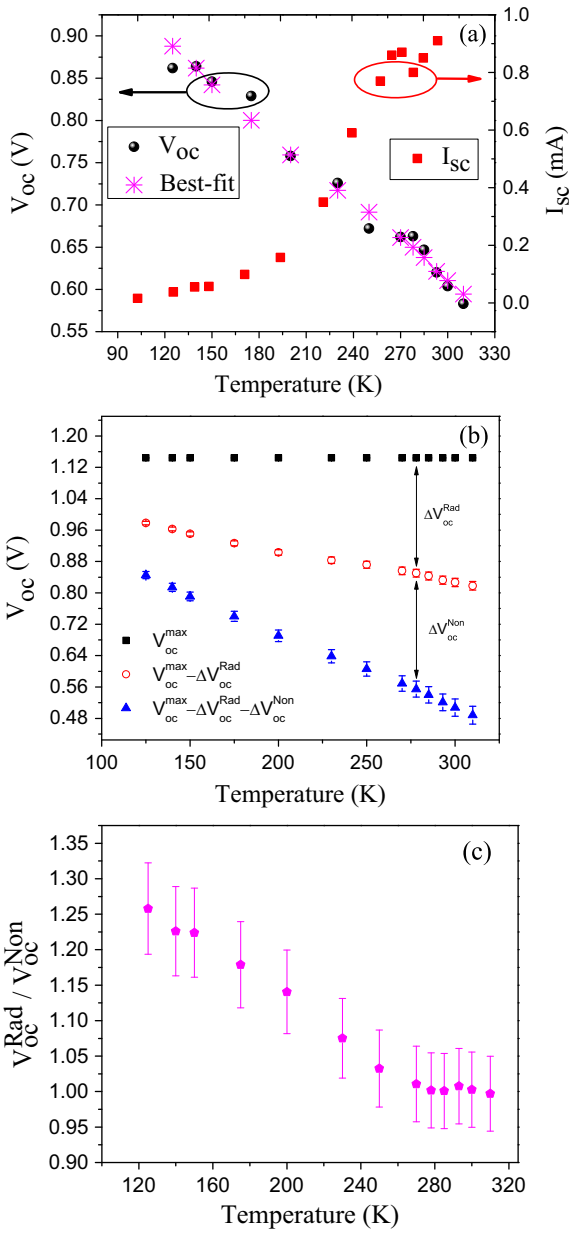

Fig. 7. (a) Figure of the measured open-circuit voltage (V_{oc}) and short-circuit current (I_{sc}) as a function of temperature. Eq. (6) was used for the best-fitting of V_{oc}. (b) V_{oc} at various temperatures. (c) The ratio $\Delta V_{oc}^{rad}/\Delta V_{oc}^{non}$ as a function of temperature.

Table 1
Summary of best-fitted parameters using Eq. (6).

Parameters	Sample size (fitting times)	Mean value	SD	95% Confidence intervals
E_{CT}, eV	300	1.1	8.6×10^{-9}	$\pm 9.8\times10^{-10}$
f, eV^2		0.0069	0.0027	$\pm 3.1\times10^{-4}$
λ, eV		0.35	0.16	± 0.018
EQE_{EL}		5.6×10^{-6}	2.6×10^{-6}	$\pm 2.9\times10^{-7}$

fitting uniqueness, leading to the maximum achievable $V_{oc}=1.1$ V. For comparison, E_g of our PbS-TBAI is ca. 1.4 eV [12,23] since the smaller E_{CT} does not limit exciton dissociation [40]. As shown in Fig. 7(b), the decrease in V_{oc} through radiative and non-radiative recombination was extracted using Eqs. (7a) and (7b). The maximum V_{oc} exhibits insignificant change within our experimental temperature range, consistent with results reported by Gruber et al. [43]. Therefore, the maximum V_{oc} determined by E_{CT} is henceforth considered to be constant. Both radiative and non-radiative recombination V_{oc} losses decrease when temperature decreases. Furthermore, Fig. 7(c) shows that ΔV_{OC}^{rad} and ΔV_{OC}^{non} have similar magnitudes, although radiative recombination seems to overtake non-radiative recombination as the dominant recombination mechanism for V_{oc} loss at low temperatures, as expected. The maximum V_{oc} will be theoretically achieved at 0 K [40]. It should be noted that if CT state emission is negligible, the maximum V_{oc} is determined by the bulk energy band gap E_g. Overall, according to the above theoretical model, in order to increase the CQD solar cell V_{oc}, E_{CT} should be enhanced in future QD photovoltaic device design. In addition, taking our solar cells as an example, it is also suggested to passivate ZnO/PbS-TBAI interface traps states through proper chemical ligands to decrease the non-radiative recombination induced V_{oc} loss.

4. Results and discussion

As shown in Fig. 7(a), despite the enhanced non-radiative recombination, short-circuit current increases with increasing temperature. To extract carrier hopping transport parameters through best-fits to the six I-V curves at different temperatures, Fig. 4, two independent best-fitting computation programs were used to investigate the reliability and thus the uniqueness of the best-fitted results in a statistical analysis. These programs have been used successfully in earlier multi-parameter fits to experimental data from an amorphous/crystalline silicon solar cell heterojunction [46]. The *'mean-value best fit'* minimizes the mean square variance between the experimental data and the theoretical values. The *'statistical best fit'* uses the fminsearchbnd solver [47] to minimize the sum of the squares of errors between the experimental and calculated data. This program delivers different results due to different trial starting points generated by the program itself, thereby creating standard deviations (SD) or variances of the theoretical curve best-fitting procedure to the experimental points. To investigate the reliability of the fitted parameters, this procedure was repeated several hundred times and the 100 lowest variances were selected. Based on these 100 best-fitted results, the variance and 95% confidence interval were calculated. The statistical mean value was used as reliability (uniqueness) measure and the variance as a precision measure of the associated parameter. It is seen that the results from the two independent best-fitting programs are in very good-to-excellent agreement. In Table 2, the best-fitted values of both D_h and D_s decrease monotonically with decreasing temperature, which is consistent with the multi-phonon assisted hopping mechanism [2,26,48–50] and are close to the reported values [29,50] between 0.003 and 0.012 cm^2/s for PbS CQDs which were surface passivated with different ligands. Similar to temperature-dependent electron mobility in a two-dimensional quantum dot superlattice [32] (electron mobility increase with temperature), the electron and hole mobilities, μ_h and μ_s, decrease monotonically with decreasing temperature, which is opposite to charge carrier mobility trends in continuous energy-band structures of e.g. inorganic photovoltaic materials. It has been found [33,34] that the hopping conductivity of CdSe or PbSe quantum dot arrays increases with temperature in the range from 10 K to 523 K, due to the increase of electron mobilities by means of multi-phonon assisted hopping. Fig. 8 shows Arrhenius plots of $[T\mu_j(T)/D_j(T)]$, $j=h,s$, a combination of terms identified in Eq. (5a) which replaces the conventional Einstein relation in the CQD hopping transport theory. These figures experimentally prove the validity of the hopping Einstein relation and extract heterojunction, Fig. 8(a), and Schottky barrier inside the SCL, Fig. 8(b),

Table 2
Summary of best-fitted parameters.

Fitted parameters		Temperature, K											
		300		250		230		200		150		100	
		Mean-value best fit	Statistical best fit	Mean-value best fit	Statistical best fit	Mean-value best fit	Statistical best fit	Mean-value best fit	Statistical best fit	Mean-value best fit	Statistical best fit	Mean-value best fit	Statistical best fit
Hopping diffusivity	D_h, cm^2/s	3.66×10^{-4}	$3.52 \times 10^{-4} \pm 1.44 \times 10^{-5}$	2.52×10^{-4}	$2.36 \times 10^{-4} \pm 2.74 \times 10^{-5}$	1.17×10^{-4}	$1.09 \times 10^{-4} \pm 2.06 \times 10^{-5}$	7.74×10^{-5}	$6.48 \times 10^{-5} \pm 1.28 \times 10^{-5}$	4.74×10^{-5}	$4.11 \times 10^{-5} \pm 6.36 \times 10^{-6}$	3.61×10^{-5}	$3.53 \times 10^{-5} \pm 1.49 \times 10^{-6}$
	D_S, cm^2/s	3.77×10^{-4}	$3.94 \times 10^{-4} \pm 2.46 \times 10^{-5}$	8.43×10^{-5}	$8.32 \times 10^{-5} \pm 2.88 \times 10^{-5}$	6.76×10^{-6}	$2.07 \times 10^{-5} \pm 1.60 \times 10^{-5}$	3.56×10^{-7}	$5.87 \times 10^{-7} \pm 4.52 \times 10^{-7}$	2.30×10^{-7}	$2.51 \times 10^{-7} \pm 4.83 \times 10^{-8}$	1.21×10^{-7}	$1.28 \times 10^{-7} \pm 9.57 \times 10^{-9}$
Diffusion length	L_h, cm	3.38×10^{-6}	$3.93 \times 10^{-6} \pm 8.63 \times 10^{-7}$	4.13×10^{-6}	$3.73 \times 10^{-6} \pm 6.56 \times 10^{-7}$	3.68×10^{-6}	$3.96 \times 10^{-6} \pm 2.75 \times 10^{-7}$	3.22×10^{-6}	$3.85 \times 10^{-6} \pm 6.41 \times 10^{-7}$	3.94×10^{-6}	$4.18 \times 10^{-6} \pm 2.53 \times 10^{-7}$	4.75×10^{-6}	$5.11 \times 10^{-6} \pm 3.66 \times 10^{-7}$
	L_s, cm	5.12×10^{-6}	$5.73 \times 10^{-6} \pm 6.24 \times 10^{-7}$	3.08×10^{-6}	$3.53 \times 10^{-6} \pm 5.63 \times 10^{-7}$	5.12×10^{-6}	$4.54 \times 10^{-6} \pm 6.08 \times 10^{-7}$	3.37×10^{-6}	$2.80 \times 10^{-6} \pm 5.93 \times 10^{-7}$	2.65×10^{-6}	$2.45 \times 10^{-6} \pm 3.23 \times 10^{-7}$	5.71×10^{-6}	$5.49 \times 10^{-6} \pm 2.25 \times 10^{-7}$
Hopping mobility	μ_h, cm^2/Vs	3.41×10^{-3}	$3.29 \times 10^{-3} \pm 1.34 \times 10^{-4}$	1.33×10^{-3}	$1.25 \times 10^{-3} \pm 1.45 \times 10^{-4}$	3.83×10^{-4}	$3.23 \times 10^{-4} \pm 6.32 \times 10^{-5}$	2.09×10^{-4}	$1.85 \times 10^{-4} \pm 3.50 \times 10^{-5}$	8.15×10^{-5}	$8.63 \times 10^{-5} \pm 1.37 \times 10^{-5}$	3.89×10^{-5}	$3.92 \times 10^{-5} \pm 9.20 \times 10^{-7}$
	μ_s, cm^2/Vs	5.59×10^{-3}	$5.84 \times 10^{-3} \pm 3.64 \times 10^{-4}$	1.61×10^{-3}	$1.66 \times 10^{-3} \pm 5.48 \times 10^{-5}$	1.09×10^{-4}	$1.57 \times 10^{-4} \pm 4.80 \times 10^{-5}$	5.27×10^{-6}	$7.98 \times 10^{-6} \pm 5.84 \times 10^{-6}$	1.26×10^{-6}	$1.32 \times 10^{-6} \pm 2.52 \times 10^{-7}$	6.32×10^{-7}	$6.64 \times 10^{-7} \pm 4.11 \times 10^{-8}$
Space charge width	W, cm	2.33×10^{-5}	$2.24 \times 10^{-5} \pm 1.08 \times 10^{-6}$	1.84×10^{-5}	$1.82 \times 10^{-5} \pm 1.66 \times 10^{-6}$	1.39×10^{-5}	$1.57 \times 10^{-5} \pm 1.83 \times 10^{-6}$	1.63×10^{-5}	$1.78 \times 10^{-5} \pm 1.65 \times 10^{-6}$	1.77×10^{-5}	$1.6 \times 10^{-5} \pm 1.84 \times 10^{-6}$	1.64×10^{-5}	$1.79 \times 10^{-5} \pm 1.67 \times 10^{-6}$
Photo-generated current	I_{pH}, A	8.56×10^{-4}	$8.57 \times 10^{-4} \pm 1.08 \times 10^{-14}$	6.69×10^{-4}	$6.70 \times 10^{-4} \pm 3.11 \times 10^{-13}$	4.49×10^{-4}	$4.50 \times 10^{-4} \pm 1.22 \times 10^{-6}$	2.81×10^{-4}	$2.75 \times 10^{-4} \pm 8.74 \times 10^{-6}$	1.41×10^{-4}	$1.37 \times 10^{-4} \pm 4.3 \times 10^{-6}$	5.82×10^{-5}	$5.75 \times 10^{-5} \pm 1.28 \times 10^{-6}$
Lifetime	τ_h, s	3.12×10^{-8}	4.39×10^{-8}	6.77×10^{-8}	5.88×10^{-8}	1.16×10^{-7}	1.44×10^{-7}	1.34×10^{-7}	2.29×10^{-7}	3.28×10^{-7}	4.25×10^{-7}	6.25×10^{-7}	7.39×10^{-7}
	τ_s, s	6.95×10^{-8}	8.33×10^{-8}	1.13×10^{-7}	1.50×10^{-7}	3.88×10^{-6}	9.96×10^{-7}	3.19×10^{-5}	1.34×10^{-5}	3.05×10^{-5}	2.39×10^{-5}	2.69×10^{-4}	2.36×10^{-4}

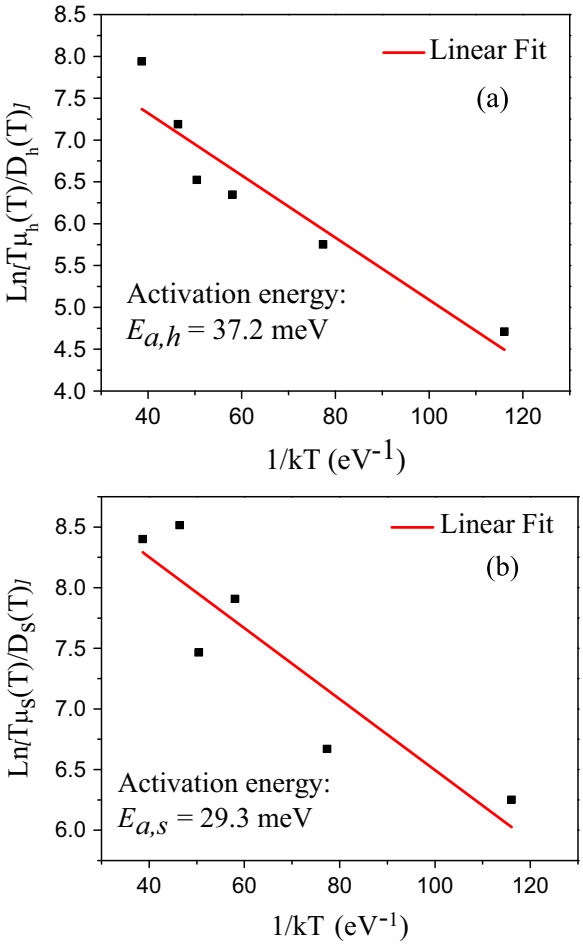

Fig. 8. Arrhenius plots of (a) the ratio $T\mu_h(T)/D_h(T)$ and (b) the ratio $T\mu_s(T)/D_s(T)$. The mobilities and diffusivities were calculated and fitted for the PbS-TBAI and the PbS-EDT interface, respectively.

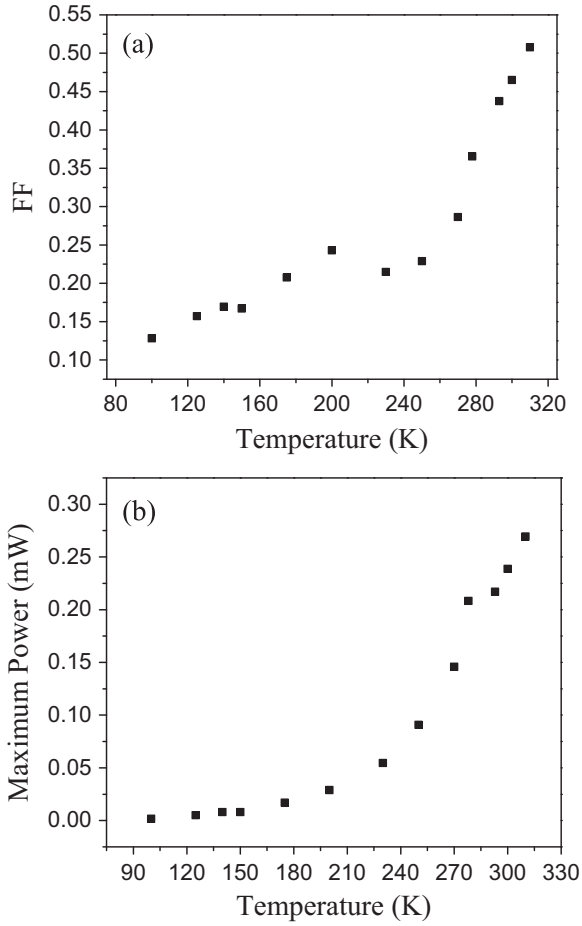

Fig. 9. (a) The CQD solar cell *FFs* measured at various temperatures. (b) Maximum power of as-studied CQD solar cell measured at various temperatures.

activation energies $E_{a,h}$=37.2 meV and $E_{a,s}$=29.3 meV, respectively.

From the fitted parameters in Table 2 using Eq. (4), the following explanation emerges: at low temperatures the charge carrier extraction efficiency is reduced due to the reduced hole mobility, however, the enhanced influence of the Schottky barrier on hole extraction, Fig. 2, reduces the hole current. The overall effect is a decrease in short-circuit current with decreasing temperature. Hopping transport of charge carriers in CQD nanolayers is a multi-phonon-assisted process [26,48,50]. As a consequence, the extraction efficiency of charge carriers, including free electrons and holes, is suppressed at low temperatures owing to the reduced thermal energy. In Fig. 9(a), the *FF* calculated from $FF=\frac{P_{max}}{V_{oc}I_{sc}}$, where P_{max} is the maximum power calculated from the I-V curves, is reduced from 0.51 at 310 K to 0.13 at 100 K as a result of reduced charge carrier extraction efficiency.

The imbalance of hole mobility in the heterojunction (PbS-TBAI) and in the associated Schottky diode (PbS-EDT) gives rise to S-shaped and negative exponential current-voltage curves, as shown in Fig. 4. In Table 2, the best-fitted values of carrier mobilities μ_h and μ_s, at 300 K show that μ_h is smaller than μ_s, implying sufficiently high charge carrier extraction rate in the hole extraction layer (PbS-EDT). This results in holes being able to be extracted efficiently and, as a result, the CQD solar cell behaves like a normal one-diode device. The best-fitted results reveal better photovoltaic material made of PbS-EDT than of PbS-TBAI. This is also consistent with the SCL lower mobility activation energy $E_{a,s}$ across the Schottky barrier, Fig. 8(b), than $E_{a,h}$ across the heterojunction, Fig. 8(a). A similar conclusion in terms of electron mobility was reported by ref. [50] using frequency-domain photocarrier radiometry (PCR). However, due to the complicated device architecture, each of the two fitted mobilities leading to the Einstein plots of Fig. 8(a) and (b) should not be unconditionally interpreted to be exclusively associated with the PbS-TBAI or PbS-EDT interfaces. Although at 250 K the fitted $\mu_s > \mu_h$, the 250 K I-V characteristic shapes in Figs. 4(b) and 5(a) reveal that low mobility of charge-carrier-induced hole accumulation on the anode side has already set in, thereby reducing hole extraction efficiency. This trend is further demonstrated at even lower temperatures by the fitted results which show that μ_h and μ_s magnitudes reverse, with μ_h becoming larger than μ_s, especially at 100 K. However, it should be noted that both unbalanced mobility and Schottky diode contribute to the formation of anomalous I-V characteristics, although our best-fitted results are not able to provide strong evidence of the role of the SCL electric field, the fitted values of which show high standard deviation. The existence of the reverse Schottky diode has been established in previous reports [12,15]. It is important to point out from the simulated curves shown in Fig. 5 (a) that anomalous I-V curves can appear *even without the existence of a Schottky diode*. Fig. 9(b) shows that the calculated maximum power decreases with decreasing temperature. This is consistent with both mechanisms of the imbalanced charge carrier mobilities and existence of Schottky diode, which reduce solar efficiency through hole-accumulation-induced charge carrier extraction reduction. Apart from optimizing the work functions of

the anode metal and CQD nanolayers, for instance, a smaller anode work function can alleviate the effect of Schottky diode effect in our solar cells, applying a high charge carrier mobility layer next to the anode so as to reduce the interfacial activation energy measured through the Einstein relation, Fig. 8(a), appears to be a potentially effective method for the improvement of CQD solar efficiency. The suggestion of applying high charge carrier mobility layer next to the anode is supported by the results of Zhang et al. [51] that an increased CQD solar cell PEC was achieved by employing a hole transport interlayer between the QD film and anode metal. Furthermore, based on our simulations, it is also recommended to apply graded hole transport layers close to the anode which 1) enhance the intrinsic electric field to increase the hole mobility; 2) create additional interfaces to improve exciton dissociation; 3) alleviate the Schottky diode effect to remove hole accumulation influences; and 4) further block electron flow to the anode. However, this strategy may complicate the device fabrication processes.

The photogenerated current, I_{pH}, according to the electric circuit of Fig. 3, is the sum of I_{sc} and the current flowing across the heterojunction diode. Both of these currents are controlled by temperature sensitive exciton and free charge carrier hopping transport. The best-fitted values of I_{pH} at various temperatures are shown in Table 2. I_{pH} and I_{sc} exhibit the same trend with temperature. I_{pH} depends on the dissociation of excitons as follows: when excitons are generated optically, they can dissociate into free electrons and holes through two paths. They may diffuse to the heterojunction interface where the local electric field can separate electron-hole pairs [52,53]; or they can be decoupled during hopping diffusion between neighboring quantum dots [54]. Inter-dot coupling strength is determined by ligand length: short ligand length yields strong coupling strength. However, it is possible that exciton decoupling is also thermal energy related, as more ambient thermal energy induces higher exciton vibration amplitude, increasing the decoupling probability. Excitons that do not dissociate undergo recombination through radiative and/or non-radiative processes as discussed above. Recombination contributes to the loss of excitons and consumes photogenerated current. Therefore, I_{pH} decreases at lower temperatures.

Electron (hole) lifetime τ_h (τ_s) is calculated from statistically fitted values of D_h (D_s) and L_h (L_s) through the equation: $\tau_h = \frac{L_h^2}{D_h}$. As summarized in Table 2, both τ_h and τ_s decrease with increasing temperature which is consistent with the temperature-dependent carrier lifetime reported by Wang et al. [55,56] and Mandelis et al. [26]. In these cases, excitons in both coupled and uncoupled PbS CQDs were found to possess longer lifetimes at low temperatures due to lower radiative and non-radiative recombination. Table 2 shows two calculated values of τ_h (as well as τ_s) for each temperature, obtained from '*mean-value best fit*' and '*statistical best fit*'. They exhibit small differences demonstrating high reliability and uniqueness of the measurements resulting from the proposed model. The non-monotonic trend of the electron hopping diffusion length L_h is the result of the trade-off between increased diffusivity and decreased lifetime with increased temperature, through $L_h = \sqrt{D_h \tau_h}$. Strictly speaking, the diffusion length L_h is a material property, and the intrinsic lifetime affecting factors should include trap states and dot-to-dot coupling [3,7,49,54]. Our best-fitted L_h and L_s values agree with reported values for PbS CQDs in the range between 30 nm and 230 nm [30].

The fitted SCL width W associated with hole accumulation at 300 K is larger than that at other temperatures. Note that the fitted depletion width W through Eq. (4) is an effective value across the PbS CQD layers. In other words, the actual SCL of PbS-TBAI and PbS-EDT is determined through a competitive process between the depletion layers of the heterojunction and the Schottky diode. To calculate the effective SCL, the depletion extent and width of both diodes should be considered. The increase of W at high temperatures, Table 2, is consistent with changes in the accumulated hole density at the PbS-EDT CQD/Au interface which acts as a conventional junction depletion layer. Specifically, at low temperatures, due to reduced hole extraction efficiency as discussed above, higher density of accumulated holes results in higher density of occupied local QD energy states, and therefore a narrow depletion layer. In contrast, at high temperatures, hole density at the interface decreases due to higher hole extraction efficiency, thereby, alleviating the concentration gradient and resulting in reduced density of occupied local QD energy states, and a wider depletion layer.

5. Conclusions

A theoretical model of hopping transport in PbS CQD solar cells was introduced to extract charge carrier hopping parameters including hopping diffusivity, diffusion length, mobility, space charge layer width, photogenerated current, and relaxation lifetime. A double-diode electric circuit model featuring a heterojunction (PbS-TBAI/ZnO) and a Schottky diode (PbS-EDT/Au anode) with two electric fields of opposite directions was used to quantitatively interpret experimental I-V curves obtained from a fabricated CQD solar cell with a structure: ITO/ZnO/PbS-TBAI QD/PbS-EDT QD/Au, which exhibits anomalous I-V characteristics at temperatures below 300 K. Detailed best-fits of I-V data to the theoretical model and simulations revealed that imbalanced charge carrier mobility is one of two factors giving rise to S-shaped and negative exponential I-V characteristics. The other factor is the formation of a reverse Schottky barrier for holes adjacent to the hole-extracting anode. The existence of a modified Einstein relation linking hole diffusivity and mobility and the hopping activation energy $E_{a,s}$ over the Schottky barrier was validated, leading to the measurement of $E_{a,s}$. A similar relation at the PbS-TBAI heterojunction was demonstrated and used to calculate the effective barrier activation energy $E_{a,h}$.

In addition, quantitative analysis showed that the V_{oc} of our CQD solar cell is limited by the existence of charge-transfer (CT) states located at the ZnO/PbS-TBAI interface. The loss mechanism responsible for V_{oc} decrease was attributed to both radiative and non-radiative recombination processes which provided quantitative insight into the nature of the V_{oc} temperature dependence. The present model and I-V analysis can be used to measure device transport parameters, especially hopping mobility, aimed at minimizing Schottky barrier in order to maximize the short-circuit current and P_{max}, toward the optimization of CQD solar cell fabrication.

Acknowledgments

The authors are grateful to the Natural Sciences and Engineering Research Council of Canada (NSERC) for a Discovery grant to AM, and to the Canada Research Chairs program.

References

[1] M. Graetzel, R.A. Janssen, D.B. Mitzi, E.H. Sargent, Materials interface engineering for solution-processed photovoltaics, Nature 488 (2012) 304–312.
[2] P. Guyot-Sionnest, Electrical transport in colloidal quantum dot films, J. Phys. Chem. Lett. 3 (2012) 1169–1175.
[3] H.W. Hillhouse, M.C. Beard, Solar cells from colloidal nanocrystals: fundamentals, materials, devices, and economics, Curr. Opin. Colloid Interface Sci. 14

(2014) 245–259.
[4] I.J. Kramer, E.H. Sargent, Colloidal quantum dot photovoltaics: a path forward, ACS Nano 5 (2011) 8506–8514.
[5] Z. Ning, X. Gong, R. Comin, G. Walters, F. Fan, O. Voznyy, E. Yassitepe, A. Buin, S. Hoogland, E.H. Sargent, Quantum-dot-in-perovskite solids, Nature 523 (2015) 324–328.
[6] E.H. Sargent, Infrared quantum dots, Adv. Mater. 17 (2005) 515–524.
[7] J. Tang, E.H. Sargent, Infrared colloidal quantum dots for photovoltaics: fundamentals and recent progress, Adv. Mat. 23 (2011) 12–29.
[8] E.H. Sargent, Colloidal quantum dot solar cells, Nat. Photonics 6 (2012) 133–135.
[9] G. Konstantatos, E.H. Sargent (Eds.), Colloidal Quantum Dot Optoelectronics and Photovoltaics, Cambridge University Press, 2013.
[10] B.A. Joyce, P.C. Kelires, A.G. Naumovets, in: Quantum Dots: Fundamentals, Applications, and Frontiers: Proceedings of the NATO ARW on Quantum Dots: Fundamentals, Applications and Frontiers, Crete, Greece 20–24 July 2003, vol. 190, Springer Science and Business Media, 2005.
[11] S.A. Mcdonald, G. Konstantatos, S. Zhang, P.W. Cyr, E.J. Klem, L. Levina, E. H. Sargent, Solution-processed PbS quantum dot infrared photodetectors and photovoltaics, Nat. Mater. 4 (2) (2005) 138–142.
[12] C.H.M. Chuang, P.R. Brown, V. Bulović, M.G. Bawendi, Improved performance and stability in quantum dot solar cells through band alignment engineering, Nat. Mater. 13 (8) (2014) 796.
[13] G.H. Kim, F.P. Garci, a de Arquer, Y.J. Yoon, X. Lan, M. Liu, O. Voznyy, Z. Yang, F. Fan, A.H. Ip, P. Kanjanaboos, S. Hoogland, J.Y. Kim, E.H. Sargent, High-efficiency colloidal quantum dot photovoltaics via robust self-assembled monolayers, Nano Lett. 15 (11) (2015) .7691–7696.
[14] A.G. Pattantyus-Abraham, I.J. Kramer, A.R. Barkhouse, X. Wang, G. Konstantatos, R. Debnath, L. Levina, I. Raabe, M.K. Nazeeruddin, M. Grätzel, E.H. Sargent, Depleted-heterojunction colloidal quantum dot solar cells, ACS Nano 4 (2010) 3374–3380.
[15] J. Gao, J.M. Luther, O.E. Semonin, R.J. Ellingson, A.J. Nozik, M.C. Beard, Quantum dot size dependent J−V characteristics in heterojunction ZnO/PbS quantum dot solar cells, Nano Lett. 11 (2011) 1002–1008.
[16] P.R. Brown, R.R. Lunt, N. Zhao, T.P. Osedach, D.D. Wanger, L.Y. Chang, M. G. Bawendi, V. Bulovic, Improved current extraction from ZnO/PbS quantum dot heterojunction photovoltaics using a MoO3 interfacial layer, Nano Lett. 11 (2011) 2955–2961.
[17] U. Würfel, D. Neher, A. Spies, S. Albrecht, Impact of charge transport on current-voltage characteristics and power-conversion efficiency of organic solar cells, Nat. Comm. 6 (2015) 6951.
[18] J. Gao, C.L. Perkins, J.M. Luther, M.C. Hanna, H.Y. Chen, O.E. Semonin, A.J. Nozik, R.J. Ellingson, M.C. Beard, n-Type transition metal oxide as a hole extraction layer in PbS quantum dot solar cells, Nano Lett. 11 (2011) 3263–3266.
[19] A. Wagenpfahl, D. Rauh, M. Binder, C. Deibel, V. Dyakonov, S-shaped current-voltage characteristics of organic solar devices, Phys. Rev. B 82 (2010) 115306.
[20] R.W. Crisp, D.M. Kroupa, A.R. Marshall, E.M. Miller, J. Zhang, M.C. Beard, J. M. Luther, Metal halide solid-state surface treatment for high efficiency PbS and PbSe QD solar cells, Sci. Rep. 5 (2015) 9945.
[21] J.C. Wang, X.C. Ren, S.Q. Shi, C.W. Leung, P.K. Chan, Charge accumulation induced S-shape J–V curves in bilayer heterojunction organic solar cells, Org. Electron. 12 (2011) 880–885.
[22] B. Romero, G. del Pozo, B. Arredondo, J.P. Reinhardt, M. Sessler, U. Wurfel, Circuital model validation for S-shaped organic solar cells by means of impedance spectroscopy, Photovolt. IEEE J. 5 (2015) 234–237.
[23] X. Lan, O. Voznyy, A. Kiani, F.P. Garcia de Arquer, A.S. Abbas, G.-H. Kim, M. Liu, Z. Yang, G. Walters, J. Xu, M. Yuan, Z. Ning, F. Fan, P. Kanjanaboos, I. Kramer, D. Zhitomirsky, P. Lee, A. Perelgut, S. Hoogland, E.H. Sargent, Passivation using molecular halides increases quantum dot solar cell performance, Adv. Mater. 28 (2016) 299–304, http://dx.doi.org/10.1002/adma.201503657.
[24] Zhijun Ning, Oleksandr Voznyy, Jun Pan, Sjoerd Hoogland, Valerio Adinolfi, Jixian Xu, Min Li, Ahmad R. Kirmani, Jon-Paul Sun, James Minor, Kyle W. Kemp, Haopeng Dong, Lisa Rollny, André Labelle, Graham Carey, Brandon Sutherland, Ian Hill, Aram Amassian, Huan Liu, Jiang Tang, Osman M. Bakr, Edward H. Sargent, Air-stable n-type colloidal quantum dot solids, Nat. Mater. 13 (8) (2014) 822–828.
[25] C.H.M. Chuang, A. Maurano, R.E. Brandt, G.W. Hwang, J. Jean, T. Buonassisi, V. Bulović, M.G. Bawendi, Open-circuit voltage deficit, radiative sub-bandgap states, and prospects in quantum dot solar cells, Nano Lett. 15 (2015) 3286–3294.
[26] A. Mandelis, L. Hu, J. Wang, Quantitative Measurements of Charge Carrier Hopping Transport properties in Depleted-Heterojunction PbS colloidal quantum dot solar cells from temperature dependent current-voltage characteristics, 2016 (unpublished).
[27] H.E. Roman, L. Pavesi, Monte Carlo simulations of the recombination dynamics in porous silicon, J. Phys.: Condens. Matter 8 (1996) 5161–5187.
[28] W. Tress, A. Petrich, M. Hummert, M. Hein, K. Leo, M. Riede, Imbalanced mobilities causing S-shaped IV curves in planar heterojunction organic solar cells, Appl. Phys. Lett. 98 (2011) 063301.
[29] N. Kholmicheva, P. Moroz, E. Bastola, N. Razgonieva, J. Bocanegra, M. Shaughnessy, Z. Porach, D. Khon, M. Zamkov, Mapping the exciton diffusion in semiconductor nanocrystal solids, ACS Nano 9 (2015) 2926–2937.
[30] G.H. Carey, A.L. Abdelhady, Z. Ning, S.M. Thon, O.M. Bakr, E.H. Sargent, Colloidal quantum dot solar cells, Chem. Rev. 115 (2015) 12732–12763.
[31] N. Kasamatsu, T. Kada, A. Hasegawa, Y. Harada, T. Kita, Effect of internal electric field on InAs/GaAs quantum dot solar cells, J. Appl. Phys. 115 (2014) 083510.
[32] S. Xu, D. Thian, S. Wang, Y. Wang, F.B. Prinz, Effects of size polydispersity on electron mobility in a two-dimensional quantum-dot superlattice, Phys. Rev. B 90 (2014) 144202.
[33] D. Yu, C. Wang, B.L. Wehrenberg, P. Guyot-Sionnest, Variable range hopping conduction in semiconductor nanocrystal solids, Phys. Rev. Lett. 92 (2004) 216802.
[34] H.E. Romero, M. Drndic, Coulomb blockade and hopping conduction in PbSe quantum dots, Phys. Rev. Let. 95 (2005) 156801.
[35] W. Shockley, H.J. Queisser, Detailed balance limit of efficiency of p-n junction solar cells, J. Appl. Phys. 32 (1961) 510–519.
[36] S.M. Sze, Physics of Semiconductor Devices, John Wiley & Sons, New York, 2005.
[37] P. Würfel, U. Würfel, Physics of Solar Cells: From BASIC Principles to Advanced Concepts, 2nd ed., Wiley-VCH, Weinheim, 2009.
[38] A. Luque, A. Marti, in: A. Luque, S. Hegedus (Eds.), Handbook of Photovoltaic Science and Engineering, Wiley, West Sussex, 2003.
[39] A. Luque, A. Martí, L. Cuadra, Thermodynamics of solar energy conversion in novel structures, Phys. E: Low Dimens. Syst. Nanostruct. 14 (2002) 107–114.
[40] N.C. Giebink, G.P. Wiederrecht, M.R. Wasielewski, S.R. Forrest, Thermodynamic efficiency limit of excitonic solar cells, Phys. Rev. B 83 (2011) 195326.
[41] K. Vandewal, K. Tvingstedt, A. Gadisa, O. Inganäs, J.V. Manca, Relating the open-circuit voltage to interface molecular properties of donor: acceptor bulk heterojunction solar cells, Phys. Rev. B 81 (2010) 125204.
[42] L. Koster, S.E. Shaheen, J.C. Hummelen, Pathways to a new efficiency regime for organic solar cells, Adv. Energy Mater. 2 (2012) 1246–1253.
[43] M. Gruber, J. Wagner, K. Klein, U. Hörmann, A. Opitz, M. Stutzmann, W. Brütting, Thermodynamic efficiency limit of molecular donor-acceptor solar cells and its application to diindenoperylene/C60-based planar heterojunction devices, Adv. Energy Mater. 2 (2012) 1100–1108.
[44] P. Peumans, A. Yakimov, S.R. Forrest, Small molecular weight organic thin-film photodetectors and solar cells, J. Appl. Phys. 93 (2003) 3693–3723.
[45] K. Vandewal, K. Tvingstedt, A. Gadisa, O. Inganäs, J.V. Manca, On the origin of the open-circuit voltage of polymer–fullerene solar cells, Nat. Mater. 8 (2009) 904–909.
[46] Y. Zhang, A. Melnikov, A. Mandelis, B. Halliop, N.P. Kherani, R. Zhu, Optoelectronic transport properties in amorphous/crystalline silicon solar cell heterojunctions measured by frequency-domain photocarrier radiometry: multiparameter measurement reliability and precision studies, Rev. Sci. Instr. 86 (2015) 033901.
[47] J. D'Errico. ⟨http://www.mathworks.com/matlabcentral/fileexchange/8277-fminsearchbnd–fminsearchcon⟩.
[48] V.V. Eremenko, V.A. Karachevisev, V.V. Slavin, Phonon termoactivated exciton tunneling in crystals of weak charge transfer complexes N-TCPA doped with Nd8-TCPA, Chem. Phys. 216 (1997) 1–6.
[49] I.H. Chu, M. Radulaski, N. Vukmirovic, H.P. Cheng, L.W. Wang, Charge transport in a quantum dot supercrystal, J. Phys. Chem. C. 115 (2011) 21409–21415.
[50] L. Hu, A. Mandelis, A. Melnikov, X. Lan, S. Hoogland, H.E. Sargent, Exciton hopping transport in p- and n-type PbS colloidal quantum dot thin films using frequency-and temperature-scanned photocarrier radiometry, Int. J. Thermophys. (2016) (in preparation).
[51] X. Zhang, Y. Justo, J. Maes, W. Walravens, J. Zhang, J. Liu, Z. Hens, E. M. Johansson, Slow recombination in quantum dot solid solar cell using p–i–n architecture with organic p-type hole transport material, J. Mater. Chem. A 3 (2015) 20579–20585.
[52] P.R. Brown, D. Kim, R.R. Lunt, N. Zhao, M.G. Bawendi, J.C. Grossman, V. Bulovic, Energy level modification in lead sulfide quantum dot thin films through ligand exchange, ACS Nano 8 (2014) 5863–5872.
[53] B.A. Gregg, Excitonic solar cells, J. Phys. Chem. B 107 (2003) 4688–4698.
[54] P. Moroz, N. Kholmicheva, B. Mellott, G. Liyanage, U. Rijal, E. Bastola, K. Huband, E. Khon, K. McBride, M. Zamkov, Suppressed carrier scattering in CdS-encapsulated PbS nanocrystal films, ACS Nano 7 (2013) 6964–6977.
[55] J. Wang, A. Mandelis, A. Melnikov, S. Hoogland, E.H. Sargent, Exciton lifetime broadening and distribution profiles of PbS colloidal quantum dot thin films using frequency-and temperature-scanned photocarrier radiometry, J. Phys. Chem. C 117 (2013) 23333–23348.
[56] J. Wang, A. Mandelis, Variational Reconstruction of exciton multipath deexcitation lifetime spectra in coupled PbS colloidal quantum dots, J. Phys. Chem. C 118 (2014) 19484–19491.